Estimation of instantaneous TOA albedo at 670 nm over ice clouds from POLDER multidirectional measurements

Wenbo Sun, Norman G. Loeb, and Seiji Kato

Center for Atmospheric Sciences, Hampton University, Hampton, Virginia, USA

[1]   An algorithm that determines the 670-nm top-of-atmosphere (TOA) albedo of ice clouds over ocean using Polarization and Directionality of the Earth's Reflectance (POLDER) multidirectional measurements is developed. A plane-parallel layer of ice cloud with various optical thicknesses and light scattering phase functions is assumed. For simplicity, we use a double Henyey-Greenstein phase function to approximate the volume-averaged phase function of the ice clouds. A multidirectional reflectance best-fit match between theoretical and POLDER reflectances is used to infer effective cloud optical thickness, phase function and TOA albedo. Sensitivity tests show that while the method does not provide accurate independent retrievals of effective cloud optical depth and phase function, TOA albedo retrievals are accurate to within ∼3% for both a single layer of ice clouds or a multilayer system of ice clouds and water clouds. When the method is applied to POLDER measurements and retrieved albedos are compared with albedos based on empirical angular distribution models (ADMs), zonal albedo differences are generally smaller than ∼3%. When albedos are compared with those on the POLDER-I ERB and Cloud product, the differences can reach ∼15% at small solar zenith angles.   *INDEX TERMS:* 0360 Atmospheric Composition and Structure: Transmission and scattering of radiation; 3359 Meteorology and Atmospheric Dynamics: Radiative processes; 3360 Meteorology and Atmospheric Dynamics: Remote sensing; *KEYWORDS:* POLDER multidirectional measurement, ice clouds, albedo, angular distribution model

1.   Introduction

[2]   The Earth's climate is driven and modulated by the distribution of radiation within the Earth-atmosphere system. One of the most important parameters controlling both global and regional climate is the top-of-atmosphere (TOA) albedo. Since satellites cannot directly measure albedo due to their narrow field-of-view (FOV), the conversion of measured radiances to instantaneous albedos is needed to determine the Earth's radiation budget [*Wielicki et al.*, 1996]. A common approach for inferring TOA albedos from measured radiances is to use empirical scene-dependent angular distribution models (ADMs). For example, the Earth Radiation Budget Experiment (ERBE) [*Barkstrom*, 1984] used a set of 12 ADMs for converting the ERBE-measured radiances to TOA fluxes [*Smith et al.*, 1986; *Suttles et al.*, 1988]. *Loeb et al.* [2000] developed ADMs for estimating TOA albedos from the Polarization and Directionality of the Earth's Reflectance (POLDER-I) instrument [*Deschamps et al.*, 1994]. Those ADMs were defined as a function of cloud cover and optical depth but not cloud phase. More recently, ADMs for the Clouds and the Earth's Radiant Energy System (CERES) instrument [*Wielicki et al.*, 1998] on the Tropical Rainfall Measuring Mission (TRMM) were developed from coincident CERES broadband and Visible Infrared Radiometer (VIRS) narrow-band measurements. The CERES ADMs are defined by imager-derived parameters that have a strong influence on the angular variation of the radiance field [*Loeb et al.*, 2003]. Separate CERES ADMs were developed for liquid water and ice clouds.

[3]   An alternative approach is to combine multiangle radiance measurements from a scene and use a theoretical bidirectional model to infer TOA fluxes. In the current version of the POLDER-I level-2 Earth Radiation Budget (ERB) and Cloud product [*Buriez et al.*, 1997], TOA albedos as well as other cloud properties, such as cloud optical thickness, are determined from POLDER measurements for each individual viewing direction under the assumption of a plane-parallel cloud layer composed of spherical droplets with an effective radius of 10 μm and an effective variance of 0.15 [*Hansen and Travis*, 1974]. Many studies have shown that the single scattering properties of ice crystals differ substantially from those of liquid droplets [*Volkovitskiy et al.*, 1980; *Takano and Liou*, 1989; *Mishchenko et al.*, 1996; *Liou et al.*, 2000]. For ice clouds and mixed phase clouds, the assumption of spherical particles can cause large differences in the retrieved cloud physical properties [*Doutriaux-Boucher et al.*, 2000]. A

better approach is to assume an inhomogeneous hexagonal microphysics model [*Doutriaux-Boucher et al.*, 2000]. This approach will be used to infer ice cloud properties acquired by POLDER-II instrument on board the Advanced Earth Observing System-II (ADEOS-II) satellite launched in December, 2002 (F. Parol, personal communication, 2003). Note here that the reason to introduce inhomogeneous inclusions in ice crystals in light scattering calculations is to obtain a featureless phase function. The featureless phase function can also be obtained by specifying surface roughness [e.g., *Yang and Liou*, 1998] or habit irregularity [e.g., *Sun et al.*, 2003] for ice crystals in light scattering calculations. Moreover, the volume-averaged single-scattering properties of ice clouds depend not only on particle shapes but also on number distribution of particle sizes. Although theoretical studies show that the vertical inhomogeneity of cloud particle size and shape is unimportant for cirrus bidirectional reflectance at visible wavelength [*Yang et al.*, 2001], the number distribution of particle sizes and shapes in entire cloud may still cause differences in the retrieved cloud properties.

[4] In this study, a new algorithm for estimating TOA albedos over ice clouds is introduced. The method, called the Multidirectional Reflectance Matching (MRM) method, is applied to POLDER multidirectional 670-nm measurements but can also be used with multidirectional measurements from other instruments such as the Multiangle Imaging Spectroradiometer (MISR) and the Along Track Scanning Radiometer (ATSR). In the following, an overview of the MRM method is presented. We first apply the algorithm to a hypothetical ice cloud to verify that the method works for a theoretical test case, and then apply the MRM method to POLDER measurements and compare MRM albedos with (1) albedos in the POLDER-I Level-2 ERB and cloud product [*Buriez et al.*, 1997] and (2) albedos inferred from the ADMs described by *Loeb et al.* [2000].

2. POLDER Data

[5] The POLDER instrument [*Deschamps et al.*, 1994] flew onboard the ADEOS-I polar orbiting platform from August 1996 to June 1997. POLDER is based on a two-dimensional charged coupled device (CCD) detector array, a rotating wheel carrying spectral and polarized filters, and wide field of view optics. On a Sun-synchronous orbit with an altitude of 797 km, POLDER has a swath width of ~2200 km and a pixel size of ~6 km × 7 km at nadir. As the ADEOS satellite passes over a scene, up to 14 successive measurements are acquired from various viewing geometries in eight narrow spectral bands between 443 nm and 910 nm. POLDER calibration uncertainty is estimated to be smaller than 3−4% [*Hagolle et al.*, 1999]. The "ERB, water vapor, and clouds" processing line results [*Buriez et al.*, 1997] in the POLDER-I level 2 products are averaged over 9 by 9 original POLDER pixels resulting in "super-pixels" with a spatial resolution of ~60 km × 60 km. This processing line provides cloud parameters such as cloud fraction and cloud phase, as well as solar and viewing geometries which are necessary for inverting radiances to fluxes. Cloud fraction is determined by applying a cloud detection algorithm to each full-resolution pixel and viewing direction [*Parol et al.*, 1999]. Cloud phase is determined

using the differences in polarized reflectance at 865 nm between liquid water and ice clouds in different scattering angle ranges [*Goloub et al.*, 2000]. In this study, the multiple-angular radiance measurements at 670 nm from overcast ice cloud super-pixels over ocean are used.

3. Multidirectional Reflectance Matching (MRM) Albedo Retrieval Algorithm

3.1. Retrieval of Albedo

[6] While it is always possible to find a cloud model that matches one single bidirectional observation of a given target, it is not so easy to model the complete set of multi-angular observations. Using a database of theoretical TOA radiances at 670 nm for various combinations of phase functions and cloud optical depth, the MRM method searches the database to find the cloud model that provides the best match to multiangle POLDER data over each super-pixel. For a set of instantaneous POLDER multidirectional measurements, we search through the database for the cloud model that provides the minimum value of the following parameter:

$$s^2(\theta_0, \tau, p) = \sum_{n=1}^{N_d} \{wt(\theta_0, \theta_n, \varphi_n)[R_m(\theta_0, \theta_n, \varphi_n) - R_t(\theta_0, \theta_n, \varphi_n, \tau, p)]\}^2,$$

(1)

where R_m and R_t are the measured and theoretical reflectances, N_d is the number of the POLDER measurements used in the retrieval, θ_n and φ_n are the viewing zenith and azimuth angles for a given viewing geometry, and τ and p denote the optical thickness and phase function, respectively. Here $wt(\theta_0, \theta_n, \varphi_n)$ is the matching weight function and is described in next section. Since we avoid using the measurements whose glint angles are smaller than 10°, the number of POLDER measurements used in the retrieval can be smaller than the actual number of the POLDER measurements.

[7] The searching process can provide the best-fit reflectances $R_t (\theta_0, \theta, \varphi, \tau, p)$ and narrowband albedo $A_t (\theta_0, \tau, p)$. The best-fit anisotropic factor [*Loeb et al.*, 2000] can then be calculated as:

$$\alpha_t(\theta_0, \theta, \varphi, \tau, p) = \frac{R_t(\theta_0, \theta, \varphi, \tau, p)}{A_t(\theta_0, \tau, p)}.$$

(2)

[8] The theoretical anisotropic factor is applied to each adopted measured reflectance to estimate the narrowband albedo at that viewing angle. The retrieved albedo $A(\theta_0, \tau, p)$ is calculated as an average of the narrowband albedos estimated at different viewing angles as follows:

$$A(\theta_0, \tau, p) = \frac{1}{N_d} \sum_{n=1}^{N_d} \frac{R_m(\theta_0, \theta_n, \varphi_n)}{\alpha_t(\theta_0, \theta_n, \varphi_n, \tau, p)},$$

(3)

3.2. Matching Weight

[9] For different solar zenith, viewing zenith and relative azimuth angles, the sensitivity of the cloud anisotropy (or angular variation in the reflectance field) to the physical properties of a cloud is a strong function of viewing geometry. To select the "best-fit" cloud model parameters in equation (1), more weight should be assigned to reflectances in those angles where the anisotropy is more sensi-

tive to the cloud properties. The weights in the different viewing geometries are calculated from the theoretical radiance database as a function of solar zenith angle θ_0, viewing zenith angle θ, and viewing azimuth angle φ using the following expression:

$$wt(\theta_0, \theta, \varphi) = \sqrt{\frac{\sum\limits_{i=1}^{N_{opt}} \sum\limits_{j=1}^{N_{pfn}} \left[\alpha_t(\theta_0, \theta, \varphi, \tau_i, p_j) - \bar{\alpha}_t(\theta_0, \theta, \varphi)\right]^2}{N_{opt} N_{pfn}}}, \quad (4)$$

where N_{opt} and N_{pfn} denote the number of cloud optical thicknesses and the number of phase functions in the LUT, respectively; τ_i and p_j denote a given optical thickness and a given phase function in the LUT, respectively. $\bar{\alpha}_t(\theta_0, \theta, \varphi)$ is the mean theoretical anisotropic factor, which is given by:

$$\bar{\alpha}_t(\theta_0, \theta, \varphi) = \frac{\sum\limits_{i=1}^{N_{opt}} \sum\limits_{j=1}^{N_{pfn}} \alpha_t(\theta_0, \theta, \varphi, \tau_i, p_j)}{N_{opt} N_{pfn}}. \quad (5)$$

[10] It can be seen from equation (4) that at viewing geometries where the theoretical anisotropic factors are more sensitive to the cloud physical properties, the matching weights are larger.

3.3. Ice Cloud Model

[11] Ice clouds are composed mainly of ice crystals with extremely large variability in shape and size [*Heymsfield et al.*, 2002]. It is difficult, if not impossible, to find "typical" shapes and size distributions. Cloud bidirectional reflectance depends not only on microphysical properties of clouds, such as particle phases, shapes, sizes, and size distributions, but also on cloud thickness, morphology, number of layers, and surface types, etc. An operational retrieval algorithm for ice cloud albedos must involve some necessary assumptions.

[12] Here, we assume a single layer of plane-parallel cloud over ocean. The cloud layer is composed of ice crystals in the height range of 8–9 km. Without consideration for the individual particle shapes, size distributions, and single scattering properties, we use only bulk quantities to describe the optical properties of the layer of cloud. The necessary and complete parameters for this purpose are the optical thickness and the volume-averaged light scattering phase function of the cloud.

[13] For simplicity, we use a double Henyey-Greenstein phase function to approximate the volume-averaged phase function of the ice clouds. We do not imply here that the double Henyey-Greenstein phase function is the best for ice clouds. We simply use it because its three free parameters can generate a wide range of phase functions for building the theoretical lookup tables. The double Henyey-Greenstein phase function is expressed as

$$P_{dHG}(\theta) = fP_{HG}(\theta; g_1) + (1-f)P_{HG}(\theta; g_2), \quad (6)$$

where θ is the scattering angle; g_1 and g_2 are the asymmetry parameters. Here g_1 adopts positive values for forward
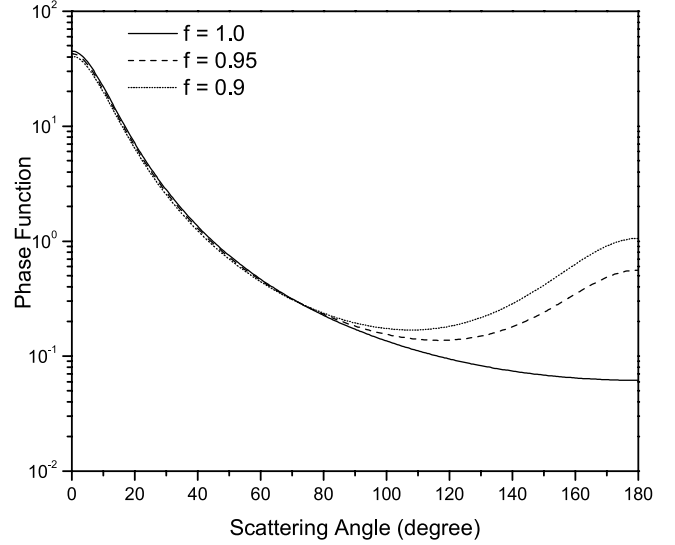

Figure 1. Double Henyey-Greenstein phase functions for $g_1 = 0.8$, $g_2 = -0.6$, and $f = 1.0$, 0.95, 0.9, respectively.

scattering peak and g_2 can be assigned a negative value to account for a backscattering peak. Here f is a positive fraction in the range [0,1]. P_{HG} is the Henyey-Greenstein phase function defined as

$$P_{HG}(\theta; g) = \frac{1 - g^2}{(1 + g^2 - 2g\cos\theta)^{3/2}}. \quad (7)$$

[14] As an example, Figure 1 shows the double Henyey-Greenstein phase functions for $g_1 = 0.8$, $g_2 = -0.6$, and $f = 1.0$, 0.95, 0.9, respectively. Using various asymmetry parameters for the forward and backward peaks and different forward and backward scattering fractions, we obtain a series of phase functions for approximating the multidirectional reflectances of ice clouds.

3.4. Lookup Table

[15] Lookup tables (LUTs) of TOA reflectances at 670 nm are constructed using the discrete ordinate radiative transfer model (DISORT) [*Stamnes et al.*, 1988]. Gas absorption, Rayleigh scattering, and aerosol effects in atmosphere are included [*Kato et al.*, 1999]. The ocean bidirectional reflectance is modeled using 6S ocean model [*Vermote et al.*, 1997] which is based upon the *Cox and Munk* [1956] algorithm. In addition, corrections to TOA radiances are applied for single-scattered radiance by ice crystals [*Nakajima and Tanaka*, 1988] and the radiance directly transmitted from the ocean surface [*Kato et al.*, 2002] to account for insufficient number of terms in Fourier expansions in DISORT. For different solar zenith angles, we produce 38 LUTs of ice cloud reflectances as function of viewing zenith angle θ, relative azimuth angle φ, and all of the input parameters. A flow chart of this process is given in Figure 2. The wind speed at sea surface is assumed to be 5 ms^{-1}. The solar zenith angle ranges from 0° to 76° with an increment of 2°. The optical thickness τ is varied linearly in log(τ) space from 0.135 to 99.48 with an increment of 0.1. The asymmetry parameter for the forward scattering
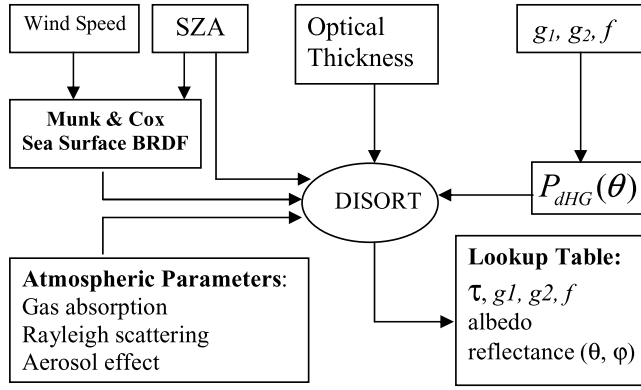
Figure 2. Procedure of making lookup tables.

peak g_1 is from 0.60 to 0.96 with an increment of 0.03. The asymmetry parameter for the backward scattering peak g_2 is set to be -0.60. The forward and backward scattering fraction f varies from 0.9 to 1.0 with an increment of 0.05. Also tabulated in the LUTs is the theoretical narrowband albedo at 670 nm determined by integrating the reflectances over the upward hemisphere.

4. Results

4.1. Sensitivity Analysis

[16] To test the validity of the MRM albedo retrieval algorithm, reflectances from DISORT for hypothetical single and multilayer ice and water clouds are used as input to the MRM algorithm at the POLDER super-pixel solar and viewing geometries during 1–10 June 1997. To ensure the accuracy of the algorithm, the retrievals throughout this study are performed only for super-pixels with more than four angular measurements. Actually, most super-pixels in POLDER data have more than four angular measurements, e.g., for ice clouds super-pixels in June 1997 only 3.13% have fewer than four angular measurements. Super-pixels within a latitude range of 60°S to 60°N and with solar zenith angles smaller than 75° are analyzed. The accuracy of the reflectance matching is determined from the relative matching error (RME) as:

$$RME = \frac{\sqrt{N_d \sum_{n=1}^{N_d} [R_m(\theta_0, \theta_n, \varphi_n) - R_t(\theta_0, \theta_n, \varphi_n, \tau_{rtv}, p_{rtv})]^2}}{\sum_{n=1}^{N_d} R_m(\theta_0, \theta_n, \varphi_n)} \times 100\%, \quad (8)$$

where τ_{rtv} and p_{rtv} are the retrieved optical thickness and phase function, respectively. We assume that the hypothetical ice cloud is confined to a layer between 8 and 9 km. The optical thickness τ is varied linearly in $\log(\tau)$ space from 0.14 to 104.6 with an increment of 0.1. The ice crystal size distribution in the cloud layer is determined from the parameterization by *Heymsfield and Platt* [1984] for the temperature range of -20 to $-25°C$. For the single layer test, ice crystals are assumed to be (1) randomized triadic Koch-fractals [*Macke et al.*, 1996] and (2) solid hexagonal columns, respectively, randomly oriented in the cloud. The

light scattering phase functions for randomized triadic Koch-fractals and solid hexagonal columns are calculated using the ray-tracing program of *Macke et al.* [1996] and the light scattering code described by *Yang et al.* [2000], respectively. The volume-averaged phase functions used in the simulation are presented in Figure 3. The volume-averaged asymmetry parameters of this cloud layer are 0.728 for randomized triadic Koch-fractals and 0.794 for solid hexagonal columns, respectively, at the wavelength of 670 nm. The wind speed at the ocean surface is assumed to be 1 ms^{-1}.

[17] The MRM algorithm calculates the relative matching error (RME) for each super pixel. The super pixel number accumulates in corresponding RME bin to produce a distribution of RME. Figure 4 shows the RME distribution for the single-layer hypothetical cloud. For the assumed clouds composed of randomized triadic Koch-fractals, the RME remains less than 2% for most cases. However, for
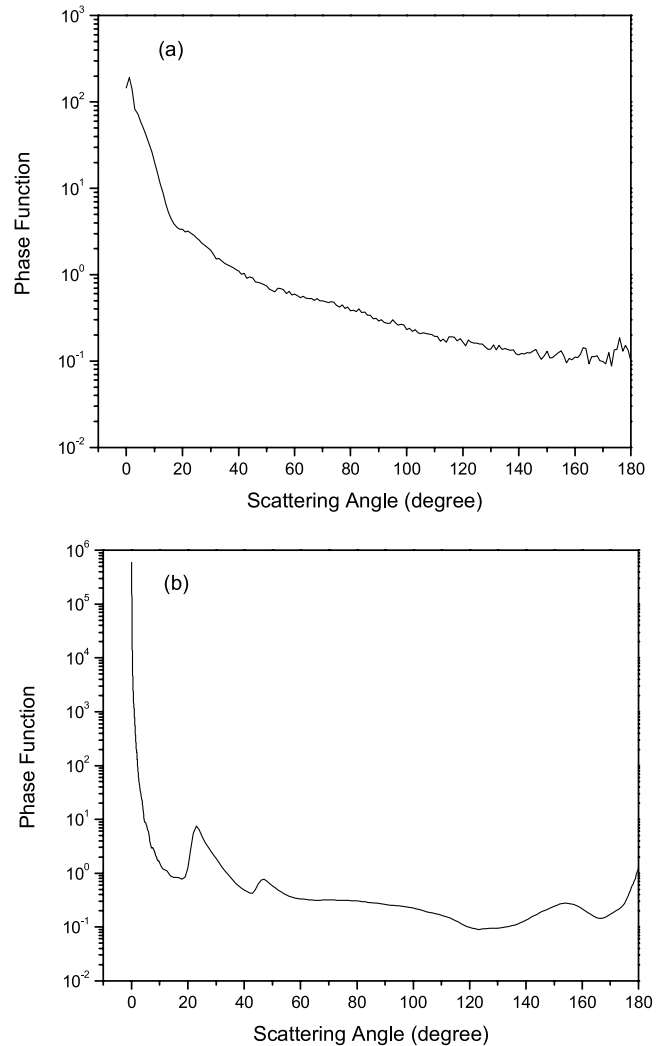

Figure 3. The volume-averaged phase functions calculated using the size distribution presented by *Heymsfield and Platt* [1984] for the temperature range of -20 to $-25°C$. The ice crystal shapes are assumed to be (a) randomized triadic Koch-fractals and (b) solid hexagonal columns, respectively.
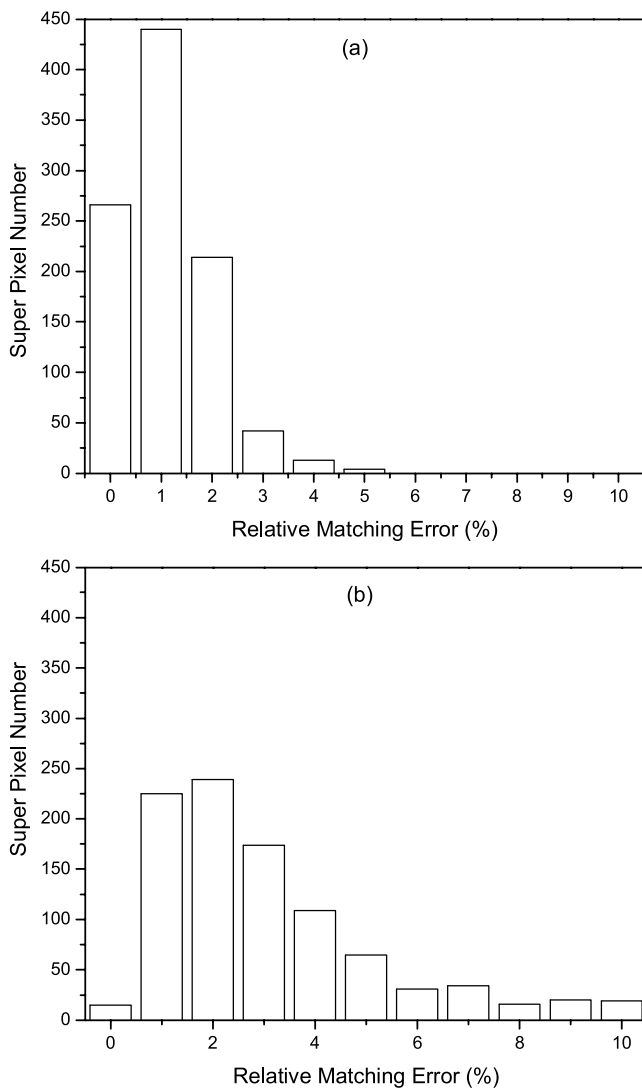
Figure 4. The relative matching error distributions for the assumed clouds composed of (a) randomized triadic Koch-fractals and (b) solid hexagonal columns, respectively.

shows the true asymmetry factor and the retrieved asymmetry factors as a function of the true optical thicknesses for the single-layer hypothetical cloud case. There is very little correlation between the true and retrieved asymmetry factors. Moreover, Figure 6 shows that the retrieved cloud optical thicknesses are underestimated by the MRM algorithm. These results suggest that the total radiance field at multiple viewing angles is insufficient to retrieve both cloud optical thickness and phase function without further constrains. Other measurements, such as polarized radiance, are needed for unambiguous retrieval of these quantities. Although the MRM algorithm does not work well for the retrieval of cloud optical thickness and phase function, it does provide accurate estimates of cloud albedo, as illustrated in Figure 7. The true and retrieved albedos for nearly all of the POLDER viewing geometries are very close to one another for both clouds composed of randomized triadic Koch-fractals and solid hexagonal columns. The relative
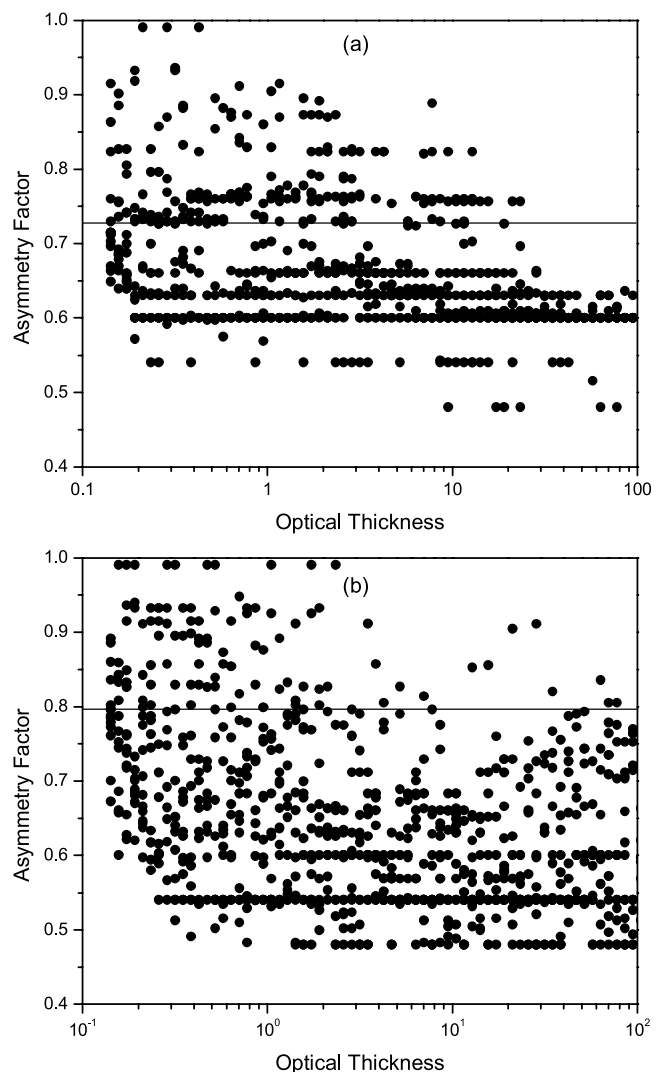
clouds composed of solid hexagonal columns, the RME is generally smaller than 5%. This is because the typical phase function for pristine ice crystals, which shows halo peaks and a strong forward- and back-scatter (Figure 3b), is significantly different from the double Henyey-Greenstein phase function. Note that an ice cloud purely composed of solid hexagonal columns is an extreme assumption. The particle growth processes in most ice clouds may result in crystal habits not very suitable for halo formation [*Wielicki et al.*, 1990; *Minnis et al.*, 1993]. There is accumulating evidence that the idealized phase function of regular hexagonal particles is not representative of the reflectance characteristics of the majority of cirrus clouds [*Mishchenko et al.*, 1996]. Real ice clouds are typically composed of particles with very complicated, highly irregular shapes [*Arnott et al.*, 1994; *Francis*, 1995]. Thus the ice cloud scattering phase functions can be rather featureless with no appreciable halos [*Foot*, 1988; *Francis*, 1995; *Gayet et al.*, 1995; *Posse and von Hoyningen-Huene*, 1995]. Figure 5

Figure 5. The true asymmetry factor (solid line) and the retrieved asymmetry factors (dots) as a function of the true optical thickness for the assumed clouds composed of (a) randomized triadic Koch-fractals and (b) solid hexagonal columns, respectively.
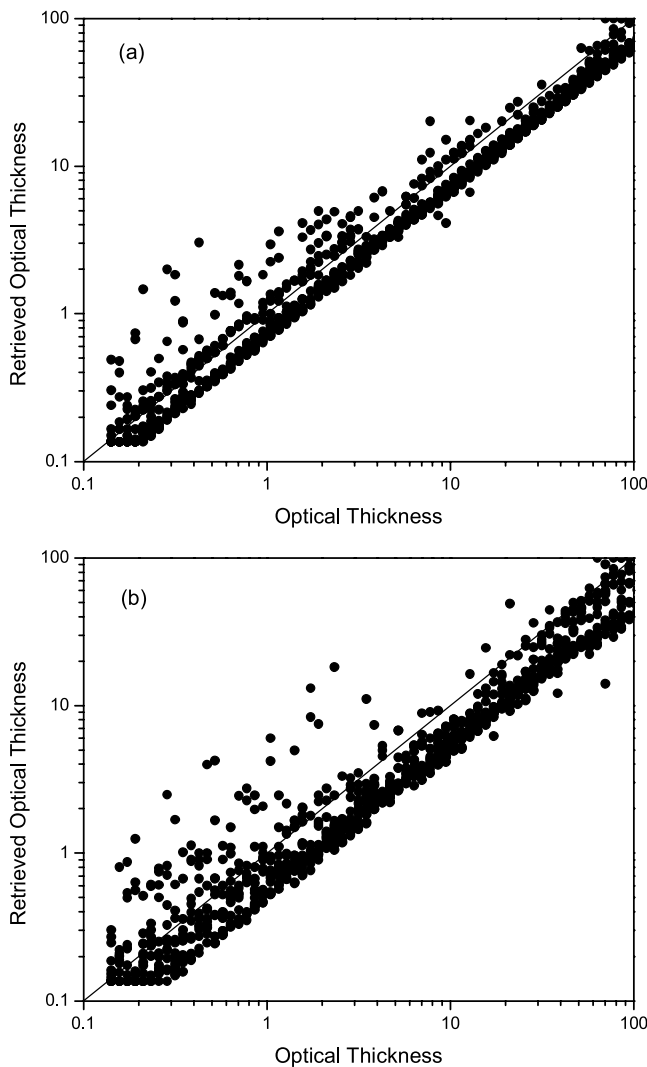
Figure 6. The comparison of the true and the retrieved optical thicknesses for the assumed clouds composed of (a) randomized triadic Koch-fractals and (b) solid hexagonal columns, respectively.

where $n(x)dx$ is the number of particles with size parameter ($2\pi r/\lambda$, where r is the radius of the droplet and λ is the incident wavelength) between x and $x + dx$. The effective size parameter, x_{eff}, is assumed to be 120 at the wavelength of 670 nm in this study, which corresponds to an effective radius of 12.8 μm. The single scattering properties of the water droplets are calculated with Mie theory. The phase function of the water cloud is shown in Figure 8a. This phase function of water clouds significantly deviates from that of ice clouds at the scattering angles of primary and secondary "rainbows."

[19] For the multilayer case, the ice cloud layer is assumed to be composed of a combination of hexagonal plates, hollow columns, bullet rosettes, and aggregates. Based on the habit percentage data from the first ISCCP regional experiment (FIRE II) intensive field observation (IFO), the following method to model the habit combinations is chosen [*Baum et al.*, 2000]. When the maximum dimension of the ice crystal is smaller than 70 μm, the ice
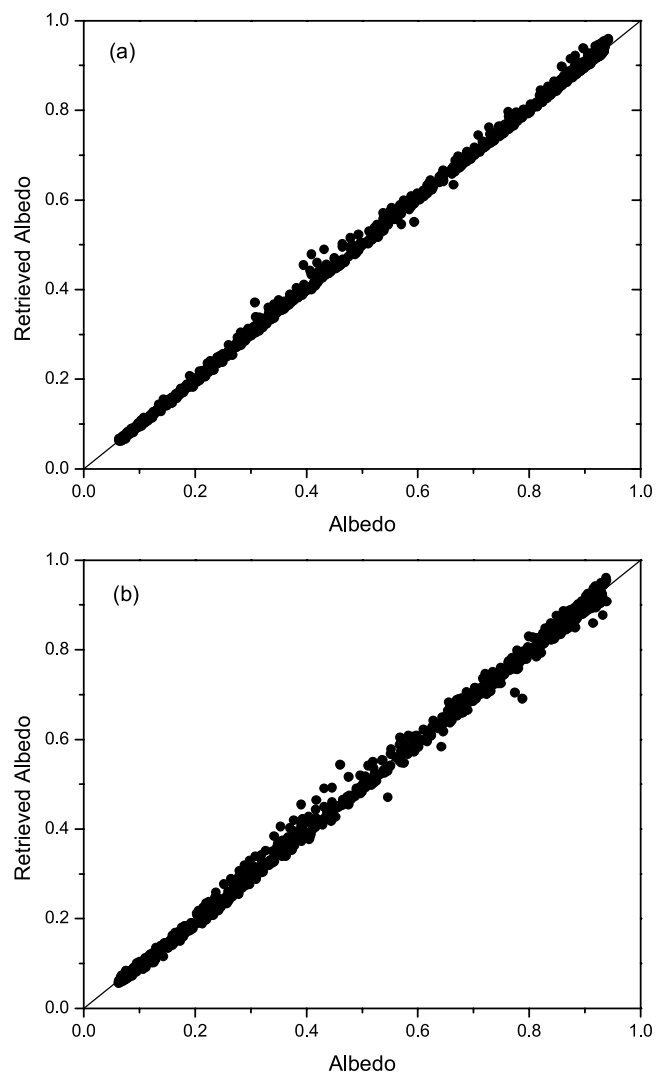

Figure 7. The comparison of the true and the retrieved ice cloud albedos for the assumed clouds composed of (a) randomized triadic Koch-fractals and (b) solid hexagonal columns, respectively.
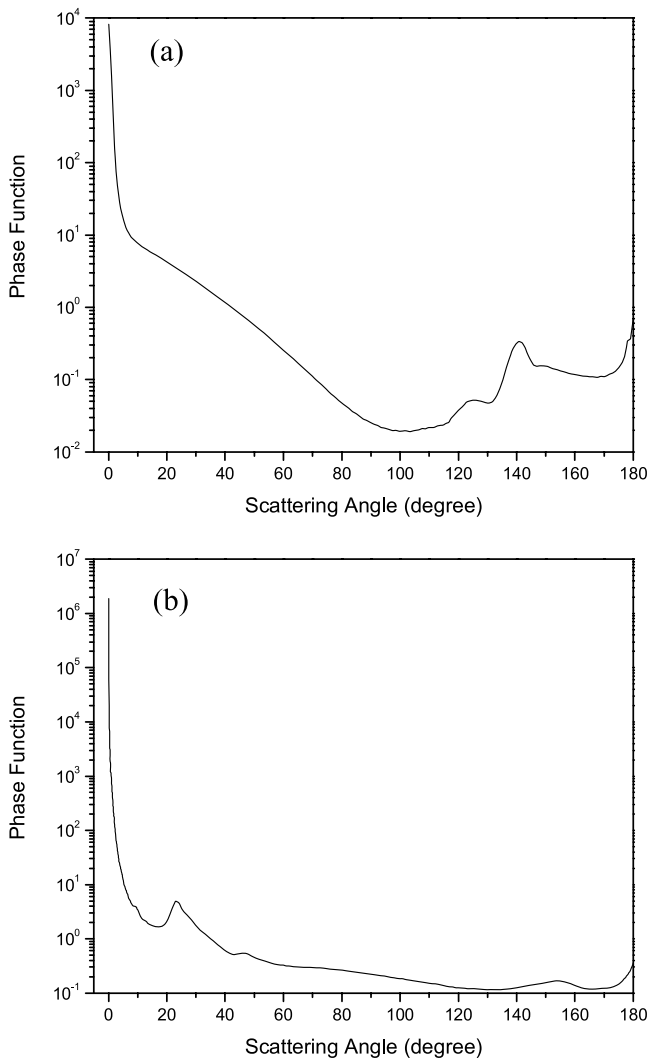
mean error and the relative RMS difference of the retrieved albedos are 0.40% and 1.96% for clouds composed of randomized triadic Koch-fractals and −1.01% and 3.00% for clouds composed of solid hexagonal columns, respectively. Note that even for the extreme clouds composed of purely hexagonal ice columns, the retrieved albedo is accurate. This means that the MRM algorithm can work well for ice clouds of various particle shapes.

[18] Surface and aircraft observations show that multiple cloud layers occur in about a half of all cloud observations, often associated with frontal areas [*Tian and Curry*, 1989; *Mace et al.*, 1997]. To examine the validity of the MRM algorithm over multilayer cloud system, we assume a water cloud layer confined in 1−2 km over ocean with a surface wind speed of 10 ms^{-1}. The water droplets in the layer of water cloud are assumed to have a size distribution as [*Hansen and Travis*, 1974]:

$$n(x) = x^6 \exp\left(-9x/x_{eff}\right), \qquad (9)$$

Figure 8. (a) Water cloud phase function and (b) ice cloud phase function used in the multilayer cloud system.

cloud optical thickness is 20, the relative mean error and the relative RMS difference of the retrieved albedos are only 0.36% and 1.19%, respectively. Larger water cloud optical thickness makes the retrieval error smaller. This also can be seen from the comparison of the RME distributions in Figures 9b and 10b.

[21] Note here that the accuracy of the albedo retrieval has little relevance with the surface wind speed. The LUTs are based on a surface wind speed of 5 m s^{-1}. However, the sample reflectance used in the sensitivity study is based on a surface wind speed of either 1 m s^{-1} or 10 m s^{-1}. We found that the surface wind speed may affect the retrieval of phase function or optical thickness, but for albedo retrieval based on MRM algorithm it does not show significant effect. On the other hand, without additional constraints the MRM algorithm cannot provide reliable phase function and cloud optical depth retrievals. However, because the error in the phase function is compensated by the error in the optical
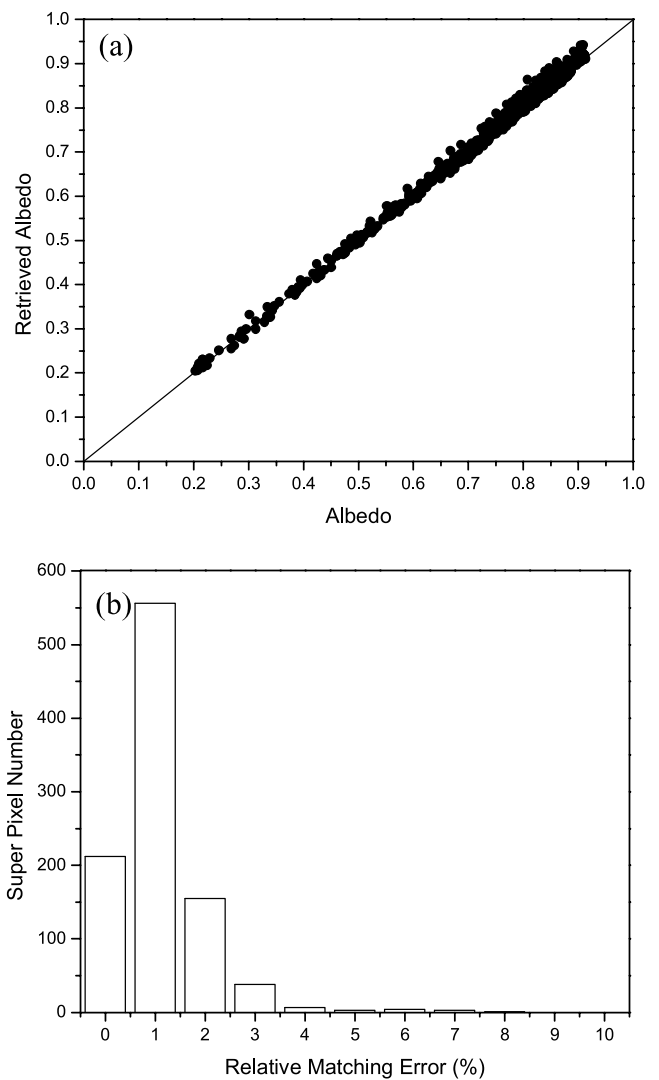
crystals within the size region is assumed to be composed of 50% bullet rosettes, 25% hexagonal plates, and 25% hollow columns. When the maximum dimension of the ice crystal is larger than 70 μm, the ice crystals within the size region is assumed to be composed of 30% aggregates, 30% bullet rosettes, 20% hexagonal plates, and 20% hollow columns. Other parameters for the ice clouds used in the multilayer system are identical to those for the single layer case. Figure 8b shows the phase function of the ice clouds composed of different particle shapes. The light scattering computational codes used to calculate the single scattering properties of individual ice crystals are described by *Yang et al.* [2000].

[20] Figures 9a and 10a show the comparison of the true and the retrieved cloud albedos for the assumed ice clouds over a layer of water cloud with an optical thickness of 2 and 20, respectively. The corresponding relative matching error distributions are given in Figures 9b and 10b. We can see that for ice clouds over water clouds, the MRM algorithm works well in the retrieval of albedos. When the water cloud optical thickness is 2, the relative mean error and the relative RMS difference of the retrieved albedos are 0.42% and 1.29%, respectively. When the water

Figure 9. (a) The comparison of the true and the retrieved cloud albedos for the assumed ice clouds over a layer of water cloud with an optical thickness of 2. (b) The relative matching error distribution for the assumed ice clouds over a layer of water cloud with an optical thickness of 2.

Figure 10. (a) The comparison of the true and the retrieved cloud albedos for the assumed ice clouds over a layer of water cloud with an optical thickness of 20. (b) The relative matching error distribution for the assumed ice clouds over a layer of water cloud with an optical thickness of 20.
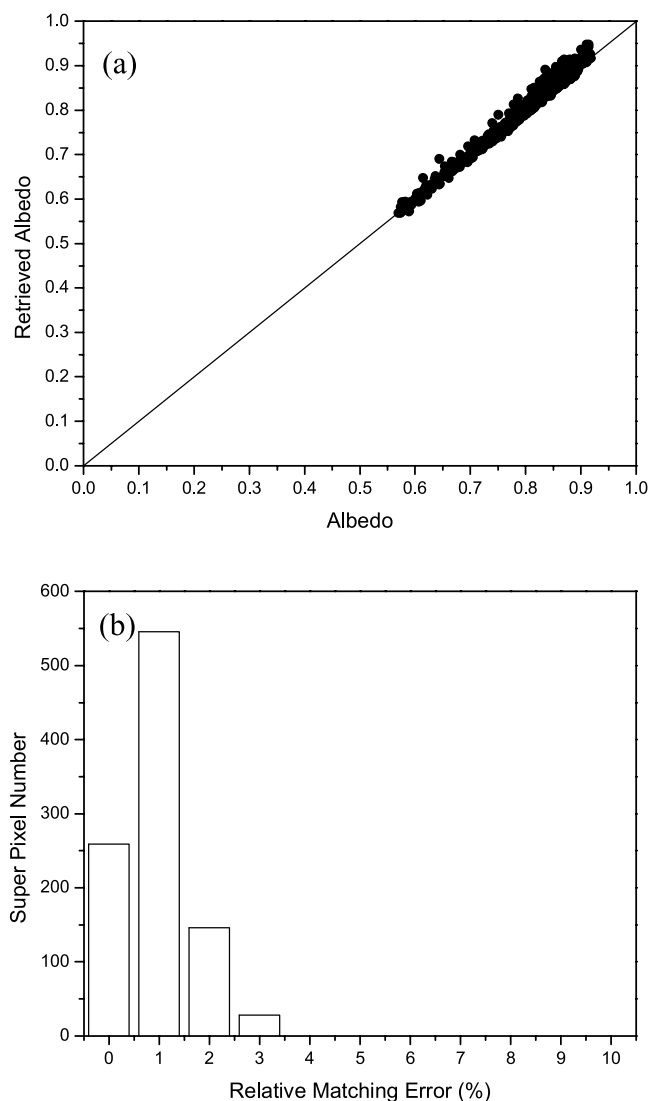
thickness, the error in the albedo is small. Therefore the retrieved optical thicknesses and phase function parameters in this study are only "effective" values that produce reasonable radiances when used in combination with one another in a radiative transfer model.

4.2. Application to POLDER Data

[22] The MRM albedo retrieval algorithm is applied to POLDER measurements of ice clouds during 1–29 June 1997 for a latitude range of 60°S to 60°N and solar zenith angles smaller than 75°. Instantaneous albedos from the MRM are compared with albedos in the POLDER-I ERB and Cloud product [*Buriez et al.*, 1997] and ADM-derived albedos [*Loeb et al.*, 2000]. Cloud albedos on the POLDER-I ERB and Cloud product are determined for each individual viewing direction under the assumption of a plane-parallel

cloud layer composed of spherical droplets [*Buriez et al.*, 1997]. These retrievals are then averaged over each pixel and angle within the super-pixel. This treatment simplifies the retrieval, but it does not take full advantage of the multidirectional measurement capability of POLDER. A more realistic light scattering phase function calculated from inhomogeneous hexagonal ice crystals [*Doutriaux-Boucher et al.*, 2000] will be used to process POLDER-II data. The ADM approach [*Loeb et al.*, 2000] uses the POLDER cloud properties as scene identification to classify empirical angular distribution models (ADMs). An albedo is inferred from each POLDER direction separately, and the directional albedos are then averaged. The ADMs are constructed by compositing radiances from many scenes measured in different satellite viewing geometries. The "percentile-τ" approach [*Loeb et al.*, 2000] defines ADMs for fixed discrete intervals of cloud fraction and uses percentile intervals of cloud optical depth to classify the ADM scene types. Albedos from the percentile-τ approach show little viewing zenith angle dependence and are in good agreement with albedos obtained by direct integration of the all-sky mean observed reflectance field [*Loeb et al.*, 2000]. However, these ADMs are not defined as a function of cloud phase and can therefore result in large instantaneous albedo errors for ice clouds in some viewing geometries [*Loeb et al.*, 2000].

[23] Figures 11a–11d show frequency distributions of instantaneous differences between POLDER and MRM albedos for solar zenith angle ranges 15°–30°, 30°–45°, 45°–60°, and 60°–75°. At solar zenith angles between 15° and 30°, POLDER albedos are much smaller than MRM values over the entire albedo range. Albedo differences are typically 0.02 but reach as high as 0.04. A 0.02 albedo difference corresponds approximately to a 13% relative difference for thin clouds (low albedos) and a 2.5% relative difference for very thick clouds (high albedos). The bias decreases with increasing solar zenith angle and generally remains below 0.01 at solar zenith angles between 60° and 75°.

[24] Figures 12a–12d show differences between ADM and MRM albedos. In most solar zenith angle ranges, the ADM and MRM results agree well on average but show more scatter about the zero line than do the albedo differences in Figure 11. The variability is especially pronounced at large solar zenith angles for clouds with moderate albedos between 0.55 and 0.7 (Figure 12d). For these clouds, relative albedo differences can reach ~10%. We must note here that the ADMs in this study are defined only as functions of cloud fraction and cloud optical thickness. *Loeb et al.* [2000] showed that the ADM sensitivity to cloud phase is most pronounced for the larger solar zenith angles (see Figure 8 of *Loeb et al.* [2000]). For thick clouds, multiple scattering dominates, and ADM-MRM albedo differences in Figure 12d are smaller. Table 1 summarizes the relative mean and RMS differences between POLDER, ADM, and MRM albedos corresponding to the distributions in Figures 11 and 12.

[25] Figure 13a shows the regional distribution of MRM ice cloud albedos between 60°S and 60°N for June 1997. The corresponding differences between the POLDER and MRM albedos and between the ADM and MRM albedos are provided in Figures 13b and 13c, respectively. The black
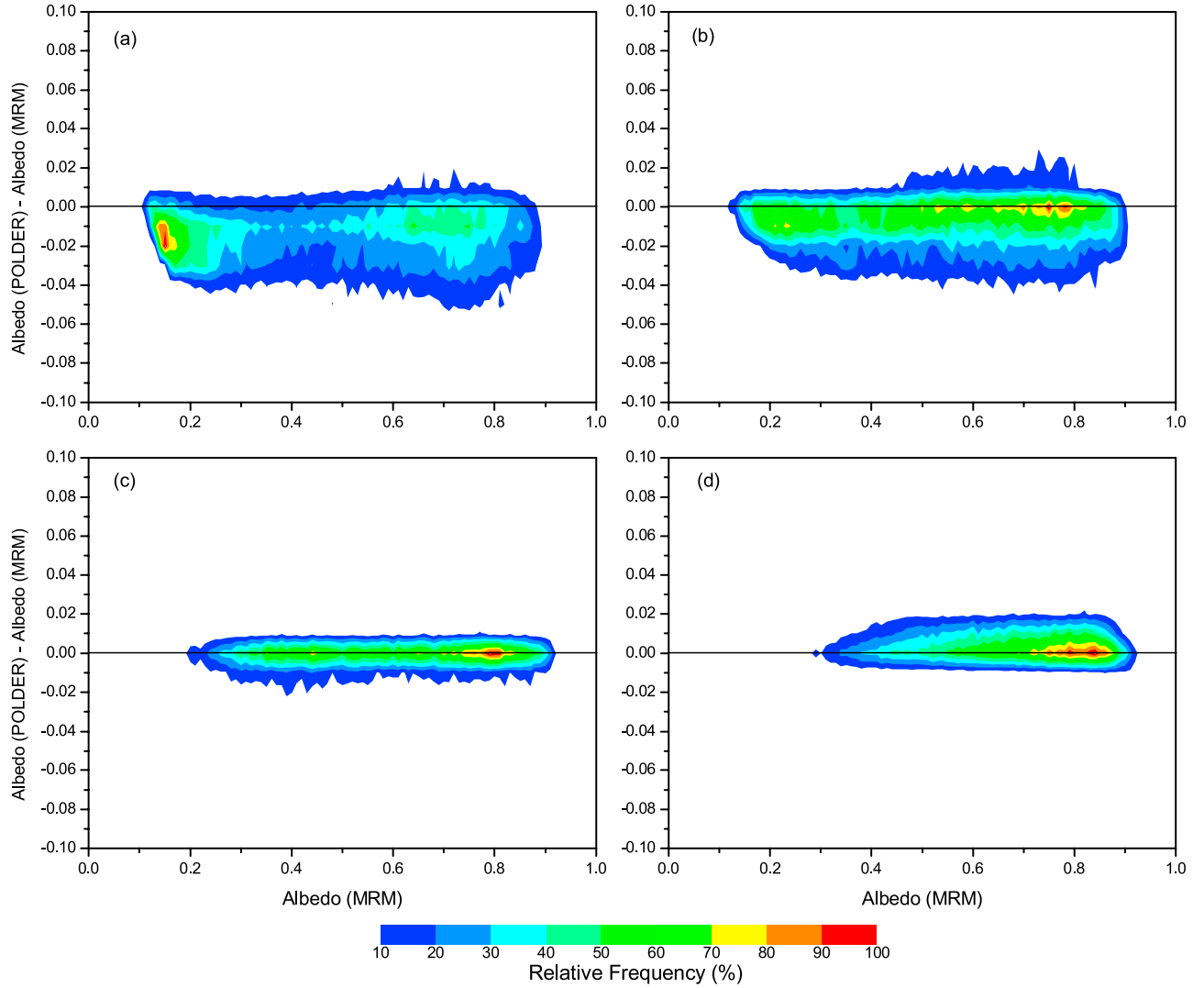
Figure 11. Relative occurrence frequency as a function of the MRM-derived albedo and the difference between the POLDER-derived and MRM-derived albedos. Figures 11a, 11b, 11c, and 11d give the results for solar zenith angle bin 15°–30°, 30°–45°, 45°–60°, and 60°–75°, respectively.

areas in these figures are the locations where no retrieval is done based on our data-selection criteria. These areas are land, water cloud region, or the locations where the solar zenith angle is larger than 75°. For each geographical location with latitude *lat* and longitude *lon*, the average cloud albedos $\overline{A}$ is determined as

$$\overline{A}(lat, lon) = \frac{\sum_{i=1}^{N} A_i(lat, lon) \cos[\theta_0(lat, lon)]_i}{\sum_{i=1}^{N} \cos[\theta_0(lat, lon)]_i}, \quad (10)$$

where N denotes the record number at the specific location, and A_i denotes the instantaneous albedo of a super pixel. We can see that the ice cloud albedos are higher in the Southern Hemisphere because in June the solar zenith angles are larger there and albedo increases with solar zenith angle. There is less ice cloud over the ocean between 30°S and the equator because this area is dominated by low-level water

clouds. The large differences between ADM- and MRM-derived instantaneous albedos observed in Figure 12d for clouds with moderate albedos are seen in Figure 13c between 30°S and 40°S. Solar zenith angles in this latitude range are generally larger than 60°.

[26] After zonally averaging, Figure 14 shows that the differences between the ADM and MRM albedos are generally negative in the Northern Hemisphere and positive in the Southern Hemisphere, whereas the differences of the POLDER-derived and the MRM-derived albedos between 30°S and 60°N are always negative. Because the differences are of opposite sign between the Northern and Southern Hemispheres, the globally averaged ADM and MRM albedos are very close and have a difference of −0.0033.

[27] Figure 15 shows the relative matching error (RME) distribution for ice cloud super pixels in June 1997 between latitude 60°S and 60°N with solar zenith angles smaller than 75°. It can be seen that most of the cases concentrate in an error range of less than 3%. The error is slightly larger than that in Figure 4a because many factors in the actual clouds may be different from the plane parallel cloud model, such
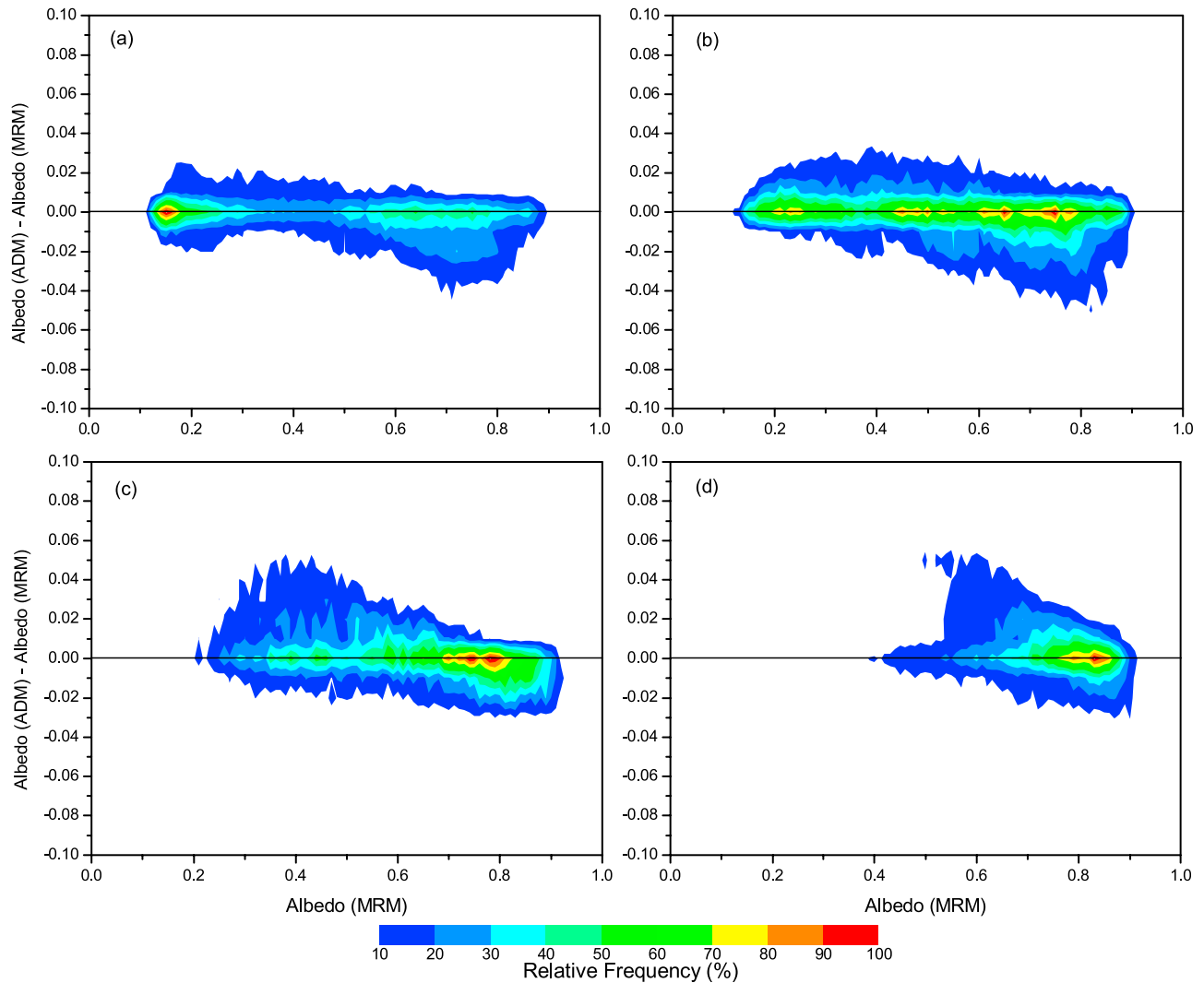
Figure 12. Similar to Figure 11, but for the ADM-derived and the MRM-derived albedos.

as the nonuniform particle distribution, cloud top morphology, cloud phase ambiguity, and multiple cloud layers, etc. However, for most of the super pixels, the matching error in Figure 15 is comparable to the calibration error of the POLDER instrument [*Hagolle et al.*, 1999]. The RME distribution for actual clouds shown in Figure 15 is significantly different from that in Figure 4b for ice clouds composed of solid hexagonal columns. This implies that actual ice clouds generally have relatively featureless light scattering phase functions rather than typical phase functions for pristine ice crystals. Note here that for the cases where ADM- and MRM-derived albedos have large differences (i.e., for solar zenith angles $60°-75°$ and MRM-derived albedos between ~0.5 and ~0.7), the matching errors are generally smaller than $\sim3\%$. It means that the matching error is not the reason for the significant albedo differences between the ADM and MRM algorithms.

5. Summary and Conclusions

[28] An algorithm for estimating TOA albedo at 670 nm over ice clouds using POLDER multidirectional measurements is developed. A plane-parallel ice cloud layer over ocean with various cloud optical thicknesses and light scattering phase functions is assumed. Lookup tables (LUTs) of cloud reflectance as a function of viewing geometry, cloud optical depth, and phase function are constructed using the DISORT program. The ice cloud phase functions consist of several combinations of parameters for the double Henyey-Greenstein phase function. Retrievals are determined by finding the combination of cloud parameters that yield the closest match to the POLDER reflectances for each POLDER super-pixel.

Table 1. Relative Mean and RMS Differences of POLDER- and ADM-Derived Albedos From MRM-Derived Albedos Corresponding to the Distributions in Figures 8–9

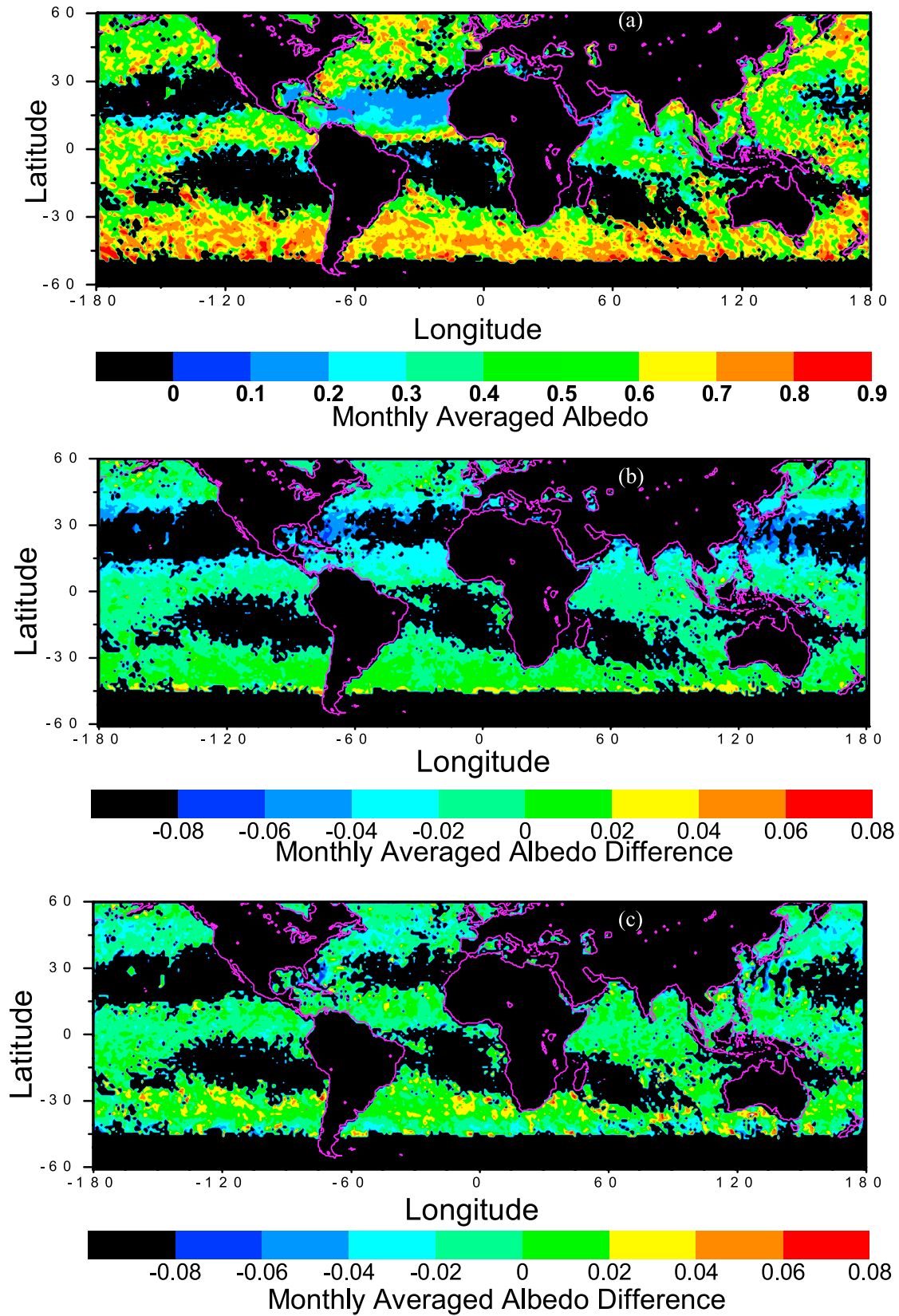| θ_0	POLDER-I ERB and Cloud Product		ADM	
	Mean, %	RMS, %	Mean, %	RMS, %
$15°-30°$	−3.361	5.806	−1.392	4.656
$30°-45°$	−1.980	4.222	−0.748	4.060
$45°-60°$	−1.012	2.406	0.164	3.832
$60°-75°$	0.431	2.360	0.985	4.514

Figure 13. The monthly mean ice cloud albedos within a latitude range of 60°S to 60°N for June 1997 (a). Also shown are the differences of the monthly mean ice cloud albedos (b) between the POLDER and the MRM and (c) between the ADM method and the MRM, respectively.
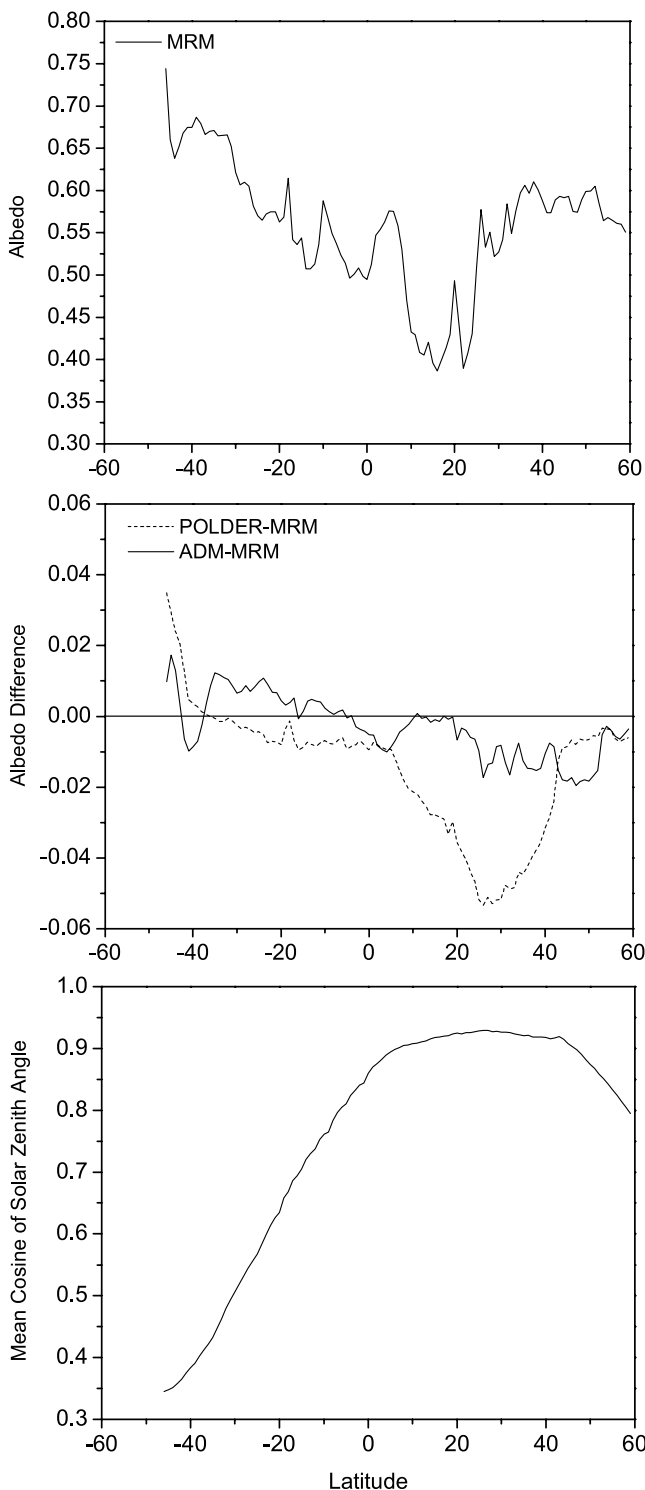
Figure 15. The relative matching error distribution for ice cloud super pixels in June 1997 between latitude 60°S and 60°N with solar zenith angles smaller than 75°.

[29] At small solar zenith angles, differences between the POLDER- and MRM-derived albedos are relatively large. We conclude that the phase function plays an important role for this trend. At small solar zenith angles, albedo is mostly determined by reflectances close to backscattering angular region and in this angular region the reflectance is more sensitive to the cloud physical properties including the phase function. Therefore at small solar zenith angles, the POLDER- and MRM-derived albedos have large differences due to the different phase functions applied. At large solar zenith angles, there are a significant number of thin clouds where the monthly mean ADM- and MRM-derived albedos have large differences. For these clouds, the MRM matching errors are still around 3%, which means the matching error is not the likely cause for these differences. The differences might be attributed to the neglect of cloud phase in the ADM scene identification. However, for globally and monthly averaged albedo, the ADM and the MRM retrieved values are similar.

[30] Future work beyond this study is to extend the MRM algorithm for the retrieval of ice cloud albedo over land based on different ground scene types. The validation results demonstrate that although the MRM algorithm can accurately retrieve the TOA albedos to within ∼3% for both a single layer of ice clouds or a multilayer system of ice clouds and water clouds, it cannot reliably retrieve cloud phase functions and optical thicknesses independently. More measured quantities (possibly the polarized radiances) might be necessary for these cloud physical property retrievals. Furthermore, in the generation of the LUTs the phase function of various ice crystal habits can be used. Using the MRM approach, it is possible to determine which habit fits the observation best, i.e., the particle shape might be retrieved.

Figure 14. The monthly and zonally mean MRM-derived albedos for June 1997 (top panel). Also shown are the differences of the monthly and zonally mean albedos between the ADM and the MRM for June 1997 (middle panel) and the monthly and zonally mean solar zenith angles for June 1997 between latitude 60°S and 60°N (bottom panel).
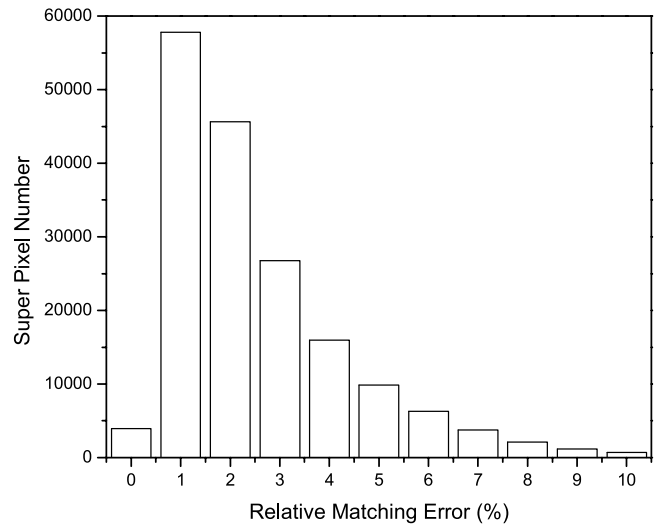
References

Arnott, W. P., Y. Y. Dong, J. Hallett, and M. R. Poellot (1994), Role of small ice crystals in radiative properties of cirrus: A case study, FIRE II, November 22, 1991, *J. Geophys. Res.*, *99*, 1371–1381.

Baum, B. A., D. P. Kratz, P. Yang, S. C. Ou, Y. Hu, P. F. Soulen, and S.-C. Tsay (2000), Remote sensing of cloud properties using MODIS airborne simulator imagery during SUCCESS: 1. Data and models, *J. Geophys. Res.*, *105*, 11,767–11,780.

Barkstrom, B. R. (1984), The Earth Radiation Budget Experiment (ERBE), *Bull. Am. Meteorol. Soc.*, *65*, 1170–1185.

Buriez, J. C., C. Vanbauce, F. Parol, P. Goloub, M. Herman, B. Bonnel, Y. Fouquart, P. Couvert, and G. Seze (1997), Cloud detection and derivation of cloud properties from POLDER, *Int. J. Remote Sens.*, *18*, 2785–2813.

Cox, C., and W. Munk (1956), Slopes of the sea surface deduced from photographs of the sun glitter, *Bull. Scripps Inst. Oceanogr.*, *6*, 401–488.

Deschamps, P. Y., F. M. Breon, M. Leroy, A. Podaire, A. Bricaud, J. C. Buriez, and G. Seze (1994), The POLDER mission: Instrument characteristics and scientific objectives, *IEEE Trans. Geosci. Remote Sens.*, *32*, 598–615.

Doutriaux-Boucher, M., J. C. Buriez, G. Brogniez, L. C. Labonnote, and A. J. Baran (2000), Sensitivity of retrieved POLDER directional cloud optical thickness to various ice particle models, *Geophys. Res. Lett.*, *27*, 109–112.

Foot, J. S. (1988), Some observations of the optical properties of clouds, II, Cirrus, *Q. J. R. Meteorol. Soc.*, *114*, 145–164.

Francis, P. N. (1995), Some aircraft observations of the scattering properties of ice crystals, *J. Atmos. Sci.*, *52*, 1142–1154.

Gayet, J.-F., O. Crepel, and J.-F. Fournol (1995), A new polar nephelometer for in situ measurements of microphysical and optical properties of clouds, in *Proceedings of the Conference on Cloud Physics*, pp. 26–30, Am. Meteorol. Soc., Boston, Mass.

Goloub, P., M. Herman, H. Chepfer, J. Riedi, G. Brogniez, P. Couvert, and G. Seze (2000), Cloud thermodynamical phase classification from the POLDER spaceborne instrument, *J. Geophys. Res.*, *105*, 14,747–14,759.

Hagolle, O., P. Goloub, P. Y. Deschamps, H. Cosnefroy, X. Briottet, T. Bailleul, J. M. Nicolas, F. Parol, B. Lafrance, and M. Herman (1999), Results of POLDER in-flight calibration, *IEEE Trans. Geosci. Remote Sens.*, *37*, 1550–1566.

Hansen, J. E., and L. D. Travis (1974), Light scattering in planetary atmospheres, *Space Sci. Rev.*, *16*, 527–610.

Heymsfield, A. J., and C. M. R. Platt (1984), A parameterization of the particle size spectrum of ice clouds in terms of the ambient temperature and the ice water content, *J. Atmos. Sci.*, *41*, 846–855.

Heymsfield, A. J., S. Lewis, A. Bansemer, J. Iaquinta, L. M. Miloshevich, M. Kajikawa, C. Twohy, and M. R. Poellot (2002), A general approach for deriving the properties of cirrus and stratiform ice cloud particles, *J. Atmos. Sci.*, *59*, 3–29.

Kato, S., T. P. Ackerman, J. H. Mather, and E. E. Clothiaux (1999), The k-distribution method and correlated-k approximation for a shortwave radiative transfer model, *J. Quant. Spectrosc. Radiat. Transfer*, *62*, 109–121.

Kato, S., N. G. Loeb, and C. K. Rutledge (2002), Estimate of top-of-atmosphere albedo for a molecular atmosphere over ocean using Clouds and the Earth's Radiant Energy System measurements, *J. Geophys. Res.*, *107*(D19), 4396, doi:10.1029/2001JD001309.

Liou, K. N., Y. Takano, and P. Yang (2000), Light scattering and radiative transfer in ice crystal clouds: Applications to climate research, in *Light Scattering by Nonspherical Particles*, edited by M. I. Mishchenko, J. W. Hovenier, and L. D. Travis, pp. 417–449, Academic, San Diego, Calif.

Loeb, N. G., F. Parol, J. C. Buriez, and C. Vanbauce (2000), Top-of-atmosphere albedo estimation from angular distribution models using scene identification from satellite cloud property retrievals, *J. Climate*, *13*, 1269–1285.

Loeb, N. G., N. Manalo-Smith, S. Kato, W. F. Miller, S. K. Gupta, P. Minnis, and B. A. Wielicki (2003), Angular distribution models for top-of-atmosphere radiative flux estimation from the Clouds and the Earth's Radiant Energy System instrument on the Tropical Rainfall Measuring Mission satellite: part I: Methodology, *J. Appl. Meteorol.*, *42*, 240–265.

Mace, G. G., T. P. Ackerman, and E. E. Clothiaux (1997), A study of composite cirrus morphology using data from 94-GHz radar and correlation with temperature and large-scale vertical motion, *J. Geophys. Res.*, *102*, 13,581–13,593.

Macke, A., J. Mueller, and E. Raschke (1996), Single scattering properties of atmospheric ice crystals, *J. Atmos. Sci.*, *53*, 2813–2825.

Minnis, P., P. W. Heck, and D. F. Young (1993), Inference of cirrus cloud properties using satellite-observed visible and infrared radiances, II, Verification of theoretical cirrus radiative properties, *J. Atmos. Sci.*, *50*, 1305–1322.

Mishchenko, M. I., W. B. Rossow, A. Macke, and A. A. Lacis (1996), Sensitivity of cirrus cloud albedo, bidirectional reflectances and optical thickness retrieval accuracy to ice particle shape, *J. Geophys. Res.*, *101*, 16,973–16,985.

Nakajima, T., and M. Tanaka (1988), Algorithms for radiative intensity calculations in moderately thick atmospheres using a truncation approximation, *J. Quant. Spectrosc. Radiat. Transfer*, *40*, 51–69.

Parol, F., J. C. Buriez, C. Vanbauce, P. Couvert, G. Seze, P. Goloub, and S. Cheinet (1999), First results of the POLDER "Earth Radiation Budget and Clouds" operational algorithm, *IEEE Trans. Geosci. Remote Sens.*, *37*, 1597–1612.

Posse, P., and W. von Hoyningen-Huene (1995), Information about scattering properties and particle characteristics of a stratiform cloud at Helgoland by remote optical measurements, *Beitr. Phys. Atmos.*, *68*, 359–366.

Smith, G. L., R. N. Green, E. Raschke, L. M. Avis, J. T. Suttles, B. A. Wielicki, and R. Davies (1986), Inversion methods for satellite studies of the Earth's radiation budget: Development of algorithms for the ERBE mission, *Rev. Geophys.*, *24*, 407–421.

Stamnes, K., S. C. Tsay, W. J. Wiscombe, and K. Jayaweera (1988), Numerically stable algorithm for discrete-ordinate-method radiative transfer in multiple scattering and emitting layered media, *Appl. Opt.*, *27*, 2502–2509.

Sun, W., T. Nousiainen, K. Muinonen, Q. Fu, N. G. Loeb, and G. Videen (2003), Light scattering by Gaussian particles: A solution with finite-difference time-domain technique, *J. Quant. Spectrosc. Radiat. Transfer*, *79–80*, 1083–1090.

Suttles, J. T., R. N. Green, P. Minnis, G. L. Smith, W. F. Staylor, B. A. Wielicki, I. J. Walker, D. F. Young, V. R. Taylor, and L. L. Stowe (1988), Angular radiation models for Earth-atmosphere system: Shortwave models, vol. 1, *Rep. RP-1184*, NASA, Washington, D. C.

Takano, Y., and K. N. Liou (1989), Solar radiative transfer in cirrus clouds. part I: Single scattering and optical properties of hexagonal ice crystals, *J. Atmos. Sci.*, *46*, 3–19.

Tian, L., and J. A. Curry (1989), Cloud overlap statistics, *J. Geophys. Res.*, *94*, 9925–9935.

Vermote, E. F., D. Tanre, J. L. Deuze, M. Herman, and J.-J. Morcrette (1997), Second simulation of the satellite signal in the solar spectrum, 6S: An overview, *IEEE Trans. Geosci. Remote Sens.*, *35*, 675–686.

Volkovitskiy, O. A., L. N. Pavlova, and A. G. Petrushin (1980), Scattering of light by ice crystals, *Atmos. Ocean. Phys.*, *16*, 90–102.

Wielicki, B. A., J. T. Suttles, A. J. Heymsfield, R. M. Welch, J. D. Spinherne, M.-L. Wu, D. O. Starr, L. Parker, and R. F. Arduini (1990), The 27–28 October 1986 FIRE IFO cirrus case study: Comparison of radiative transfer theory with observations by satellite and aircraft, *Mon. Weather Rev.*, *118*, 2356–2376.

Wielicki, B. A., B. R. Barkstrom, E. F. Harrison, R. B. Lee III, G. L. Smith, and J. E. Cooper (1996), Clouds and the Earth's Radiant Energy System (CERES): An Earth observing system experiment, *Bull. Am. Meteorol. Soc.*, *77*, 853–868.

Wielicki, B. A., et al. (1998), Clouds and the Earth's Radiant Energy System (CERES): Algorithm overview, *IEEE Trans. Geosci. Remote Sens.*, *36*, 1127–1141.

Yang, P., and K. N. Liou (1998), Single scattering properties of complex ice crystals in terrestrial atmosphere, *Contr. Atmos. Phys.*, *71*, 223–248.

Yang, P., K. N. Liou, K. Wyser, and D. Mitchell (2000), Parameterization of the scattering and absorption properties of individual ice crystals, *J. Geophys. Res.*, *105*, 4699–4718.

Yang, P., B. C. Gao, B. A. Baum, W. J. Wiscombe, Y. X. Hu, S. L. Nasiri, P. F. Soulen, A. J. Heymsfield, G. M. McFarquhar, and L. M. Miloshevich (2001), Sensitivity of cirrus bidirectional reflectance to vertical inhomogeneity of ice crystal habits and size distributions for two Moderate-Resolution Imaging Spectroradiometer (MODIS) bands, *J. Geophys. Res.*, *106*, 17,267–17,291.

―――――――――――――――

S. Kato and N. G. Loeb, Center for Atmospheric Sciences, Hampton University, Hampton, VA 23668, USA. (s.kato@larc.nasa.gov; n.g.loeb@larc.nasa.gov)

W. Sun, NASA Langley Research Center, Mail Stop 420, Hampton, VA 23681-0001, USA. (w.sun@larc.nasa.gov)